

## Development of a networked photonic-enabled staring radar testbed for urban surveillance

Jahangir, Mohammed; Griffiths, Darren; White, Daniel; Donlan, Gwynfor; Ren, Xiaofei; Kannanthara, Jithin; Singh, Yeshpal; Wayman, Joseph P.; Baker, Chris J.; Sadler, Jon P.; Reynolds, Jim; Antoniou, Michail

DOI:

[10.1049/rsn2.12524](https://doi.org/10.1049/rsn2.12524)

License:

Creative Commons: Attribution (CC BY)

*Document Version*

Publisher's PDF, also known as Version of record

*Citation for published version (Harvard):*

Jahangir, M, Griffiths, D, White, D, Donlan, G, Ren, X, Kannanthara, J, Singh, Y, Wayman, JP, Baker, CJ, Sadler, JP, Reynolds, J & Antoniou, M 2023, 'Development of a networked photonic-enabled staring radar testbed for urban surveillance', *IET Radar, Sonar & Navigation*. <https://doi.org/10.1049/rsn2.12524>

[Link to publication on Research at Birmingham portal](#)

### General rights

Unless a licence is specified above, all rights (including copyright and moral rights) in this document are retained by the authors and/or the copyright holders. The express permission of the copyright holder must be obtained for any use of this material other than for purposes permitted by law.

- Users may freely distribute the URL that is used to identify this publication.
- Users may download and/or print one copy of the publication from the University of Birmingham research portal for the purpose of private study or non-commercial research.
- User may use extracts from the document in line with the concept of 'fair dealing' under the Copyright, Designs and Patents Act 1988 (?)
- Users may not further distribute the material nor use it for the purposes of commercial gain.

Where a licence is displayed above, please note the terms and conditions of the licence govern your use of this document.

When citing, please reference the published version.




### Take down policy

While the University of Birmingham exercises care and attention in making items available there are rare occasions when an item has been uploaded in error or has been deemed to be commercially or otherwise sensitive.

If you believe that this is the case for this document, please contact [UBIRA@lists.bham.ac.uk](mailto:UBIRA@lists.bham.ac.uk) providing details and we will remove access to the work immediately and investigate.

## ORIGINAL RESEARCH

# Development of a networked photonic-enabled staring radar testbed for urban surveillance

Mohammed Jahangir<sup>1</sup>  | Darren Griffiths<sup>2</sup>  | Daniel White<sup>1</sup> | Gwynfor Donlan<sup>2</sup> | Xiaofei Ren<sup>1</sup> | Jithin Kannanthara<sup>2</sup>  | Yeshpal Singh<sup>2</sup> | Joseph P. Wayman<sup>3</sup> | Chris J. Baker<sup>1</sup> | Jon P. Sadler<sup>3</sup> | S. James Reynolds<sup>4</sup> | Michail Antoniou<sup>1</sup>

<sup>1</sup>Department of Electronic Electrical and System Engineering, University of Birmingham, Birmingham, UK

<sup>2</sup>School of Physics and Astronomy, University of Birmingham, Birmingham, UK

<sup>3</sup>School of Geography, Earth and Environmental Sciences, University of Birmingham, Birmingham, UK

<sup>4</sup>School of Biosciences, College of Life and Environmental Sciences, University of Birmingham, Birmingham, UK

## Correspondence

Mohammed Jahangir, School of Engineering, University of Birmingham, Edgbaston, Birmingham, B15 2TT, UK.  
Email: [m.jahangir@bham.ac.uk](mailto:m.jahangir@bham.ac.uk)

## Funding information

UK National Quantum Technology Hub in Sensing; EPSRC, Grant/Award Numbers: EP/T001046/1, EP/T011068/1

## Abstract

Urban surveillance of slow-moving small targets such as drones and birds in low to medium airspace using radar presents significant challenges. Detecting, locating and identifying such low observable targets in strong clutter requires both innovation in radar hardware design and optimisation of processing algorithms. To this end, the University of Birmingham (UoB) has set-up a testbed of two L-band staring radars to support performance benchmarking using datasets of target and clutter from realistic urban environment. This testbed is also providing the vehicle to understand how novel radar architectures can enhance radar capabilities. Some of the challenges in installing the radar at the UoB campus are highlighted. Detailed benchmarking results are provided from urban monostatic and bistatic field trials that form the basis for performance comparison against future hardware modification. The solution to the challenge of interfacing the radar to the external oscillators is described and stand-alone bench tests with the candidate oscillators are reported. The testbed provides a valuable capability to undertake detailed analysis of performance of Quantum photonic-enabled radar and allows for its comparison with conventional oscillator technology for surveillance of low observable targets in the presence of urban clutter.

## KEYWORDS

doppler radar, micro doppler, radar, radar clutter, radar target recognition

## 1 | INTRODUCTION

Radar surveillance of low observable targets such as slow-moving drones in the built-up urban environment is particularly challenging. There are numerous applications of counter-drone surveillance of drone traffic to aeroecology that require detecting, locating, tracking and identifying all airborne targets operating in this setting. This requires solving of the enduring problem of optimising detection of small targets in dense clutter and radar designers are continuously developing systems that can detect ever-smaller targets [1]. In strong clutter, phase noise will cause weak signals to be

masked close to zero-Doppler [2]. Understanding radar performance in realistic urban environments and developing a strategy to design hardware that can address the current limitations of radar phase noise has motivated the establishment of a dedicated staring radar testbed which is the subject of this paper. Given that in dense urban environments spatio-temporal characteristics of radar clutter along with multipath are closely dependent on the transmitter-target-receiver geometry, the focus of the testbed is also to provide a multi-static architecture. This would help to understand some of the mitigating factors that could benefit from spatially distributing the sensors.

This is an open access article under the terms of the [Creative Commons Attribution](https://creativecommons.org/licenses/by/4.0/) License, which permits use, distribution and reproduction in any medium, provided the original work is properly cited.

© 2023 The Authors. *IET Radar, Sonar & Navigation* published by John Wiley & Sons Ltd on behalf of The Institution of Engineering and Technology.

To this end, the University of Birmingham (UoB), Birmingham, UK has established a dedicated facility of two L-band staring radars that overlook a dense urban environment. The two radars, purchased from Thales, provide a 5 km coverage in range that spans  $90^\circ$  in azimuth [3, 4]. The radars can operate on their own or as a network and are able to collect data over their entire field of regard (FOR) over extended periods. The underlying driver for the testbed is to understand how novel radar architecture and advanced processing techniques can help to address some of the surveillance challenges of observing small targets in complex clutter.

The UoB facility will be able to support this ambition in a number of ways. Data collection of both opportune targets and controlled test flights over a variety of urban areas on an ongoing basis is supporting enhancements of both short dwell machine learning classifiers and techniques for long-term monitoring. The measurement data are a crucial element of benchmarking the existing characteristics of the monostatic and bistatic radars. The central hardware development will be based on replacing the existing internal oscillator with an ultra-low phase noise photonics oscillator. This will lead to the introduction of a class of Quantum clocks that can be locked to the photonics oscillators to provide highly stable oscillator clock sources. More detail on the development of the specialist Quantum based oscillators can be found in ref. [5]. The introduction of the photonics oscillators into the radar front-end also opens the way to have both radars operating as a fully coherent network that utilises disciplined photonics oscillators to aid with synchronisation.

Thus, the overall ambition with the fully operational testbed is to improve the understanding of its performance and to identify the limitations in urban environments for:

- the use of Machine Learning (ML) with radars for drone, bird and other small target detection and discrimination.
- low phase noise Quantum enabled radar for detection in high clutter.
- the use of monostatic, bistatic and multistatic characterisation and processing techniques for optimising echo strength.

The main contribution of this paper is to report on the development of the UoB facility and provide benchmark results to baseline the radar and the reference oscillators. Subsequent work will report on the operation of the radar with alternative clock sources. Section 2 provides an overview of the radar and section 3 details the infrastructure set-up at UoB. Section 4 details the protocol followed for field trials and Section 5 describes the range of processing capabilities that has been developed with data from the testbed. Section 6 presents results from monostatic and bistatic benchmarking of the testbed which form an important basis for validating the radar performance against state-of-art and novel oscillator capabilities. Section 7 presents the proposed approach for interfacing the external oscillators to the radar and reports on bench tests to baseline a series of candidate oscillators which are a prerequisite to testing fully the radar against alternative oscillators. This section also discusses the

next step in validating the testbed with these alternative reference oscillators. Finally, the overall summary is provided in Section 8.

## 2 | STARING RADAR OVERVIEW

The staring radar is a Thales L-band prototype system that uses a broad beam on transmit and a 2-D array of receivers that are digitised at the element level [4]. The transmitter is a vertical stack of eight antennas to narrow the transmit beam in elevation, providing more gain at low altitudes. The receiver array has a finite coverage in azimuth and elevation. It is a  $\sim 2$  MHz bandwidth pulse radar with  $\sim 8$  kHz Pulse Repetition Frequency (PRF). There is a total of 64 receivers arranged in a  $4 \times 16$  array providing the means to form simultaneous multiple beams on receive over its entire FOR. The fully flexible digital beam-forming also allows for null steering and other advanced beamforming implementations. These and other features are incorporated to provide higher sensitivity against low altitude, low observable targets. Table 1 lists the radar operating parameters.

The system generates raw data that are temporal samples from each receiver channel for the specified number of range bins, batched into frames of a fixed number of pulses. The output raw data are the post-matched filtered complex I/Q samples. Each frame can be either saved to a file for offline processing or streamed to the real-time processor supplied by the radar manufacturer.

The real-time processor buffers data from one or more frames depending on the Coherent Pulse Interval (CPI), weights the pulses and transforms them into the frequency domain for each channel and range bin. The data from all channels are combined to form individual beams which then result in a 4-D data cube in range, azimuth, elevation and Doppler, per CPI.

An initial threshold stage produces a list of detections per CPI. Subsequent stages refine the target position and following a tracker and classification stage, individual tracks are output with labelled track identification (ID), reported kinematics and classification attributes. Figure 1 shows the processing steps performed by the real-time processor.

**TABLE 1** Typical system parameters for UoB staring radar.

Parameter	Value
Frequency	L Band
Bandwidth	$\sim 2$ MHz
Transmit power	1–2 kW
Receiver channels	$4 \times 16$
Azimuth coverage	$90^\circ$
Elevation coverage	$60^\circ$
PRF	$\sim 8$ kHz
Update rate	$\sim 0.25$ s
Polarisation	Vertical

### 3 | TESTBED DESCRIPTION

The staring radars were installed 4 km from Birmingham city centre to operate within a dense urban environment. Several challenges were faced in finding a suitable location for the equipment which, together with the steel cabin that houses the processing servers, weighed in excess of 4 tonnes.

The site of the first radar was to be the rooftop of the 6-storey Gisbert-Kapp Building on the Edgbaston campus of UoB. Following a site survey of the roof space on this building, six potential locations were identified but some of these were already used for other experimental work and others provided poor access. In the end, one area on the western wing of the building was chosen because it offered a good coverage area for the radar. A steel frame had to be constructed to support the weight of the installation and a large crane was hired to move the equipment into place. The installation was successfully completed in November 2020 despite the social distancing restrictions brought about by the COVID-19 pandemic. Figure 2 shows images from the installation process of the first radar.

The radome at the top of the ISO container has all of the radar front end components which include the transmitter, amplifier and receiver array, which are connected via fibre link to the processing server that is housed in a rack inside the cabin (Figure 3a). As shown by the schematic in Figure 3b, the rack has two servers, *HRP0* for processing the data and *SDT0* to provide a Graphical User Interface (GUI) for controlling the radar. The network switch connects the radar servers to the UoB IT network to enable remote access to the radar.

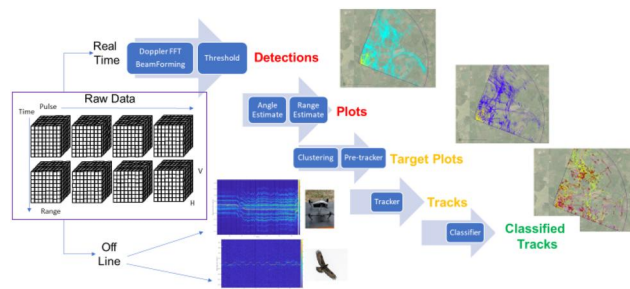


FIGURE 1 Illustration of the staring radar processing steps.

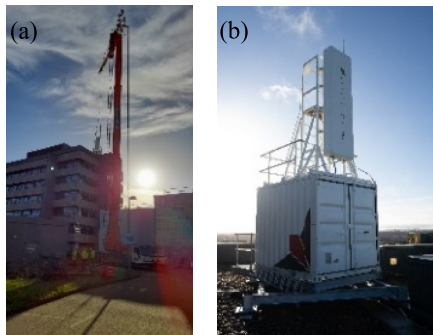


FIGURE 2 Installation of the radar on the UoB Gisbert-Kapp building. (a) A crane lifting the installation. (b) The installed Radar #1 (also known as 'GK000').

There were some additional challenges faced in selection of the location for the second radar. The sensor needed to be sited on a different building from the first radar installation to provide a sufficiently long bistatic baseline. It also had to ensure that there was reasonable overlap in the coverage of the two sensors, and simultaneously, that they were sufficiently separated to prevent saturation of the receivers by the direct signal from the adjacent radar. An initial long list of locations was reduced by considerations of the ease of access to the roof, radar line-of-site, building load-bearing integrity and any planning restrictions mandated by the UoB. The European Research Institute (ERI) was chosen from among 13 sites that were considered. Although this building is only three storeys high and obscured by tall trees (Figure 4a), the height of the radar's radome was raised by using a

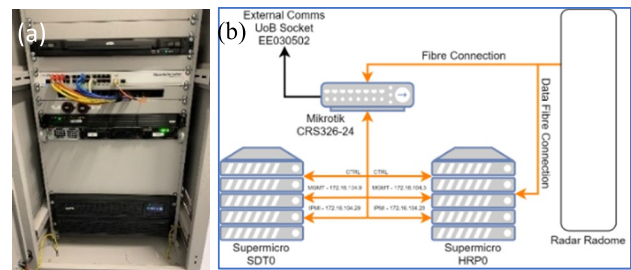


FIGURE 3 (a) The radar server rack, and (b) a schematic diagram of the radar's server network connections.

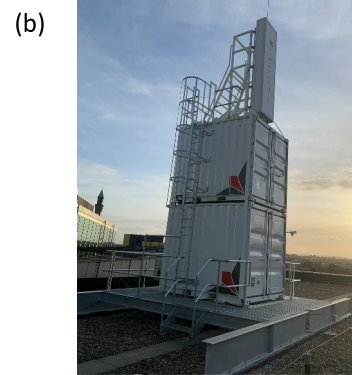
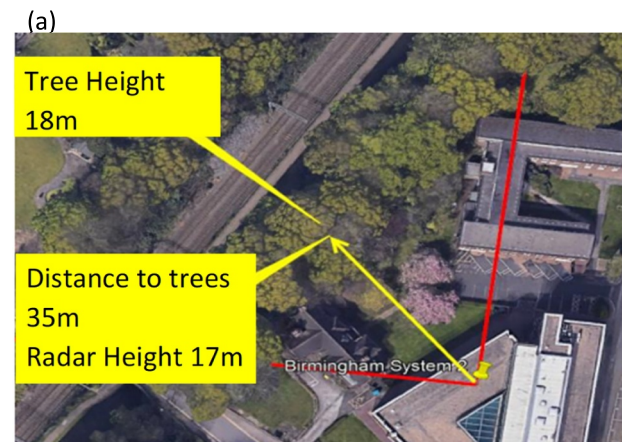


FIGURE 4 (a) The tree line blocking the radar view, and (b) Radar #2 (also known as 'GK007') with the double-cabin configuration on the roof of the ERI building at the UoB.



second cabin as a spacer. The steel frame had to be redesigned to support the additional load. The second installation was completed in November 2021 and is shown in Figure 4b.

The radar operation is controlled via a custom GUI that also allows quick visualisation of the data during live operations. Additionally, standard tools are being developed that process the data offline to benchmark the research outputs.

The raw data and processed output are stored locally on the server, and these can then be backed up onto removable storage media for offline processing. The local storage is limited to 4 TB which provides a capacity for recording radar data for 6–8 h. A dedicated storage server with several 100s TB storage capacity has been set-up with a 10 GB/s fibre link to each of two radar stations that enable raw data to be recorded over 10s of hours and backed-up in an efficient and timely manner.

Both radars are fully operational and have been run individually as monostatic systems and also as a bistatic network with free running clocks. Figure 5a shows the coverage map for both of these radars and, as can be seen by the 3-D image in Figure 5b, there are regions that are heavily built-up and therefore the location is well suited to characterise the radar measurements in a strong clutter environment. Furthermore, with overlapping coverage, a 200 m baseline, and a bistatic angle of up to  $40^\circ$  at short ranges ( $<1$  km), the facility will have the capability of collecting multistatic measurements.

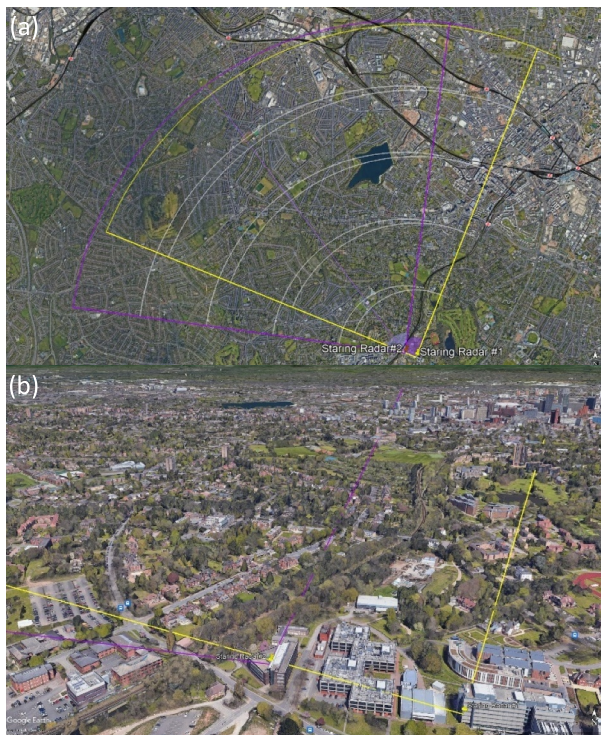


**FIGURE 5** (a) A 5-km range map showing coverage of Radar #1 (yellow) and of Radar #2 (purple) at the UoB. (b) A 3-D view of the urban area covered by the two radars.

## 4 | FIELD TRIALS PROCEDURE

Live radar trials with controlled targets form an important element of characterising radar performance, benchmarking system capabilities and collection of accurately truthed data to aid the development of machine learning classifiers ([6, 7]). Several small drones have been acquired that are routinely flown for data collection with control test targets. Techniques have also been developed to obtain accurate truth data for birds. The following sections outline the process for conducting trials with drones and birds.

### 4.1 | Control drone trials

Drone flights are performed at a variety of distances, heights and speeds to provide a diverse dataset of target signatures. The flight path is specified using waypoints that can be either pre-programmed into the drone or flown manually by an operator on linear paths between waypoints. Numerous test flights have been performed using the four rotary wing drones pictured in Figure 6a. Figure 6b is an example of a typical flight profile showing the track of GPS truth data recorded during the drone flights. Typically, the flight is performed at a fixed height, the target is landed between flights and the flight repeated in both forward and reverse directions, and at multiple heights. Some of the drone logs also provide data for the rotor speeds which can be used for generating synthetic data with very realistic looking drone micro-Doppler signatures [8].

### 4.2 | Control bird trials

Captive birds can be flown with miniaturised GPS tags to obtain good truth data which enable detailed analysis of the radar signatures from birds, in a similar manner to that used for drone targets. Previously, a Microsensory GPS tag, pictured in Figure 7a, was used to obtain truth data for captive raptors during radar trials conducted at a rural location [9]. A GPS tag was supplied by PathTrack Ltd (Otley, UK), weighed less than 5 g, measured  $31$  (L)  $\times$   $14$  (W)  $\times$   $10$  (D) mm (Figure 7b) and can record GPS data for an hour in tracking racing pigeons



**FIGURE 6** (a) Left-to-right DJI Phantom 3 (P3-D), DJI Inspire 2 (I3-D), DJI Mini Mavic 2 (M2-D), and DJI Matrice 300 (MT-D) drones. (b) Google Earth plot of GPS tracks from a control trial.

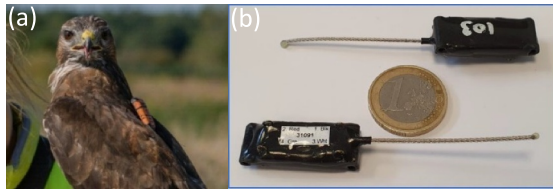


**FIGURE 7** (a) A Microsensory GPS tag deployed on a Eurasian Buzzard (*Buteo buteo*), and (b) a PathTrack nanoFix-GEO GPS logger.

(*Columba livia*) as control birds to collect radar data. In addition to supporting the development of target classifiers, these trials will also provide data from flocks of flying birds to investigate the capabilities of the radars to detect, locate and classify multiple targets.

### 4.3 | Data collection from opportune birds

By far the most data collected by the radar are from opportune targets within the radar's FOR. However, without any independent truthing, the data labelling is noisy which impacts the performance of supervised learning algorithms.

A series of line transects has been developed to truth (i.e. classify) opportune birds according to species and to match the field observations to reported track ID. The field protocol is based on an observer noting down the time at which a bird crosses an imaginary line set between the observer and a fixed target point (usually a tall feature in the landscape, such as a Church spire). The direction of flight of the bird crossing the line, the distance of the bird from the observer and the height of the bird above ground are recorded. Subsequently, assuming that only one bird crosses the transect at the time recorded, individual observations can be confidently matched to radar tracks crossing in the same direction, leading to labelled species' tracks. Figure 8 shows an example of birds being recorded on a line transect over Edgbaston Reservoir.

A number of line transects have been specified over different sites within the UoB radars' FOR at different distance bands, with plans to visit these at different times of the year to develop a truth repository for opportune birds that will provide labelling for the radar data collected by either sensor.

## 5 | PROCESSING CAPABILITIES

Between the two radars over 36 months of operation 15k hours of processed data and close to 50 TB of raw data have been recorded. This has allowed creation of large datasets (Table 2) that are helping with the development of ML classifiers. The database will continue to grow significantly over the next few years. The range of processing capabilities that has been developed with data from the test bed is presented in the following sub-sections with references to published work using data from the UoB testbed.

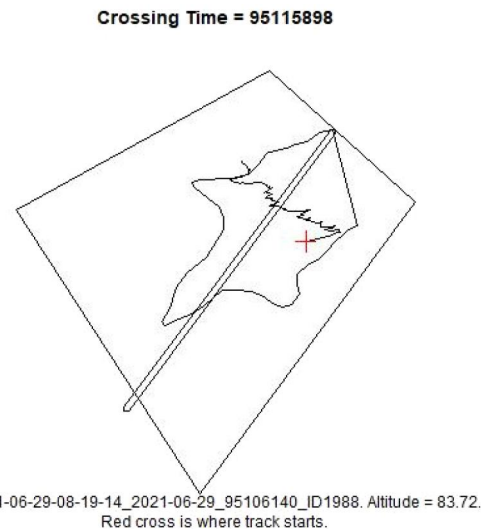


**FIGURE 8** The resultant track visualisation from an observer conducting line transect where crossing time is hour (0), minute (00), seconds (00) and milliseconds (000).

**TABLE 2** Summary of the number of flights for which spectrogram data have been generated using the UoB testbed facility's raw data.

Target	Number of Flights	Raw Data (hrs)
Bird	499	10.1
Drone	176	9.6

### 5.1 | Urban clutter characteristics

The testbed is enabling long-term observations of urban clutter. Clutter maps have been generated that plot the zero-Doppler power as a function of range and azimuth for fixed altitudes. Figure 9 compares the plots obtained with each radar taken at different times of the year.

These plots show that there is a markedly higher level of clutter on right-hand edges for Radar #1 which corresponds to high-rise city buildings. Also, there is strong clutter at around 4 km on the left that is visible in both plots. This is a multi-storey block that is in the line-of-site of both radars and provides a good location for comparative measurements of clutter strengths. These plots exhibit varying clutter intensities within the radar's FOR which provides a useful basis for observing detection sensitivities within varying clutter. The clutter maps form the central basis for benchmarking the radar performance and this is further discussed in Section 6.

### 5.2 | Drone spectrograms

Routine control trials with drones are being conducted to acquire an extensive database of representative signatures in complex clutter. The drones have been flown at different distances and in a variety of scenarios to allow for variation in



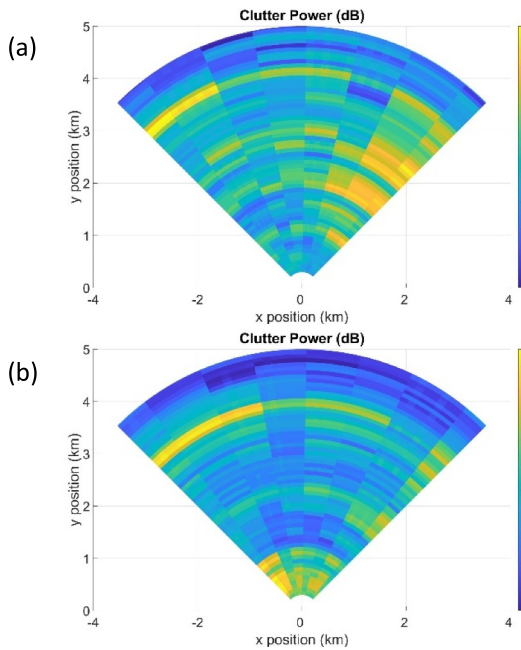


**FIGURE 9** Clutter map plotted as power in dB at zero-Doppler at 0 m height for (a) Radar #1, and (b) Radar #2. The colour bar indicates clutter power on an arbitrary scale.

Signal-to-Noise Ratio (SNR), as well as at different heights to evaluate the effects of signal occlusion due to landscape and multipath due to ground clutter reflections.

A useful way to evaluate the target signatures is to generate spectrograms of the targets. The raw data are processed to obtain range-Doppler plots for each CPI for all of the beam directions. The GPS truth data are used to specify the target range and beam direction for each CPI, and the Doppler profile for each CPI frame is concatenated to produce the spectrogram. In the spectrogram, static clutter appears at zero-Doppler and the target body Doppler will appear offset from the clutter for non-zero radial velocities.

Figure 10 compares the spectrogram obtained with each radar from the I3-D drone (Figure 6a) that flew the same pattern clockwise at a constant height of 100 m. Note that the signal is stronger and the micro-Doppler is more visible in Radar #2 and this is because of this radar having higher power and lower overall phase noise.

Figure 11 compares the spectrogram obtained from Radar #2 for a large drone (MT-D) to that of a markedly smaller drone (M2-D) (Figure 6(a)). Both drones were flown on the same nominal flight path but their signatures are markedly different. Such inter-class differences are providing the basis to distinguish between drones by model type [10].

Figure 12 shows the spectrogram generated by the MT-D drone, at three times the distance to that of the shorter-range data. As expected, the longer-range data have lower SNR with a marked reduction in the number of HELICOPTER Rotor Modulation (HERM) lines that are visible. Previous work has reported the impact of SNR on classification performance [11]. Data from the UoB testbed are progressing the work on

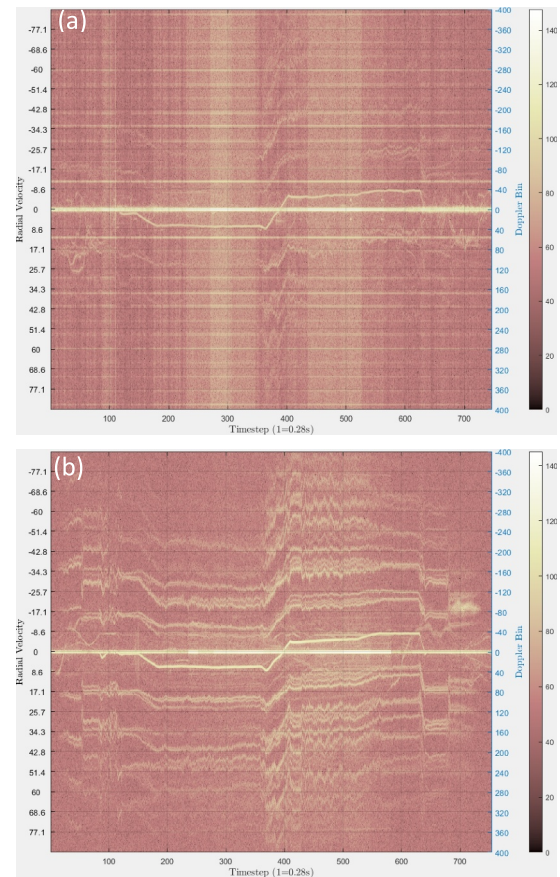


**FIGURE 10** Spectrogram of the I3-D drone from (a) Radar #1, and (b) Radar #2. The vertical axis is radial velocity in m/s and the colour scale is signal power in dB.

developing robust classifiers for challenging realistic conditions and an example of this is detailed in Table 3 from recently published results using Convolutional Neural Networks (CNN) for classifying drones and birds [12].

The testbed is being used to validate simulations that will allow the creation of datasets in volumes that are often required for deep learning ML techniques. Figure 13 is from the result reported in [8] comparing the likeliness of synthetic spectrograms generated using true rotor speeds for the I3-D drone with real spectrograms. Ongoing research is investigating how such high-fidelity simulations can reduce the reliance on real data for training and validating ML techniques.

### 5.3 | Opportune bird characteristics

Data from opportune birds are being used to populate the database in several ways. Most of this work is making use of the tracker output to filter tracks that are classified as bird and then extracting spectrograms for selected track IDs. Figure 14 shows example spectrograms for two cases. The top one is of a single bird showing an absence of any visible micro-Doppler that may be a reliable distinguishing feature from drone signatures with HERM lines (Figure 10). The bottom plot is from

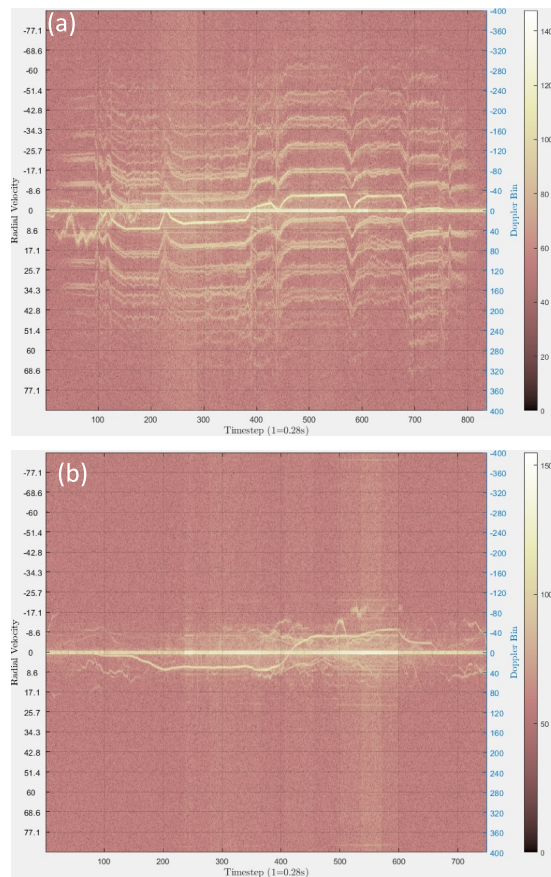


**FIGURE 11** Spectrogram from Radar #2 for (a) MT-D, and (b) M2-D drones. The vertical axis is radial velocity in m/s and the colour scale is signal power in dB.

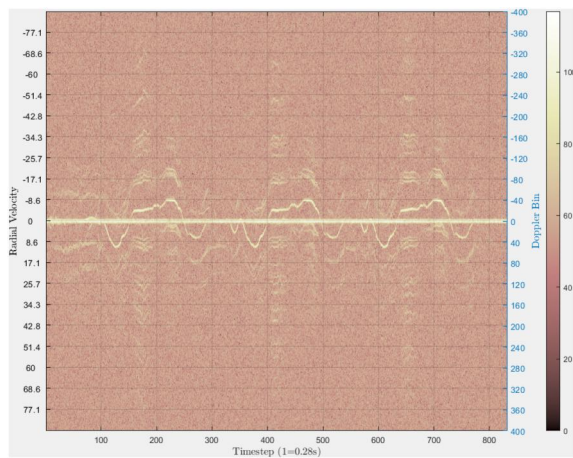


**FIGURE 12** Spectrogram of the MT-D drone at longer range with Radar #2. The vertical axis is radial velocity in m/s and the colour scale is signal power in dB.

a flock of birds and there are multiple Doppler returns which can result in the flock being confused for a drone. There has been little published work on classification of co-located multiple targets and this is a subject for future research.

Another opportunity the permanent radar installation offers is observing bird activity over long periods to map bird

**TABLE 3** Percentage accuracies recorded with CNN trained and tested on drone and bird spectrograms taken from rural and urban locations. In total analysis was performed on 7623 spectrograms of drones and birds with a 60:30:10 split between training, test and validation phases [12].

Train/Test set-up	Train (rural)	Train (rural + urban)
Test (rural)	99.8%	99.6%
Test (rural + urban)	18.3%	79.7%

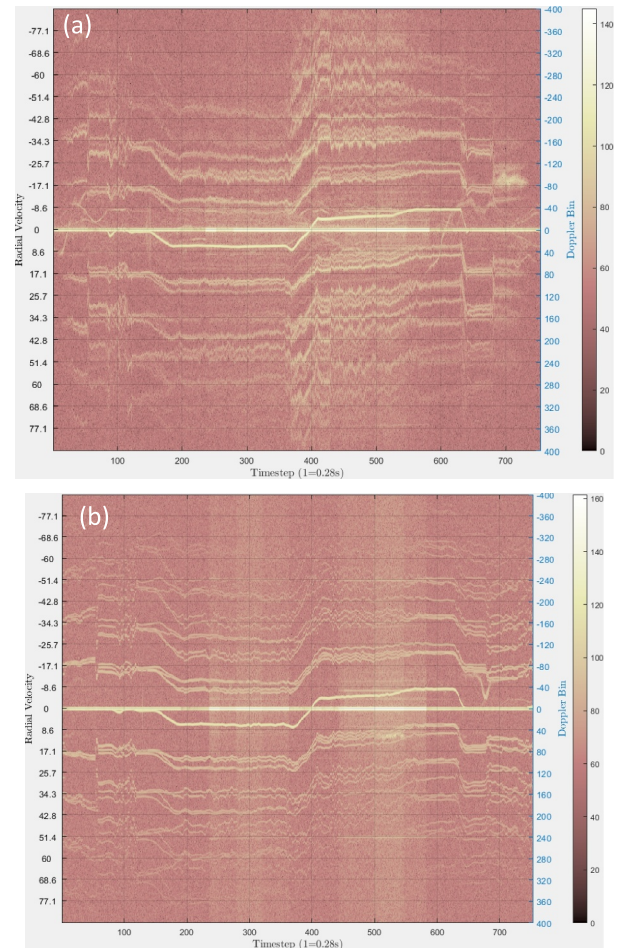


**FIGURE 13** Spectrogram of I3-D drone from (a) real data and (b) synthetic data generated using truth data from the real flight. The vertical axis is radial velocity in m/s and the colour scale is signal power in dB.

locations and movements within a dense urban setting [9]. Figure 15 compares heatmaps for two periods of the day between 04.00 and 08.00 h (GMT), and 20.00 and 23.59 h (GMT) on 10/02/2022. The latter heatmap shows much reduced bird activity whereas at dawn data show increased flighted activity. This corresponds to the time when birds enter the urban landscape from roosts (just after dawn) and when they return to roosts (after sunset). The heatmaps are being used to analyse bird activity over hours, days and weeks, and can provide a rich source of information on how birds utilise airspace in terms of number of birds aloft, spatial occupancy, altitude, and temporal patterns [13].



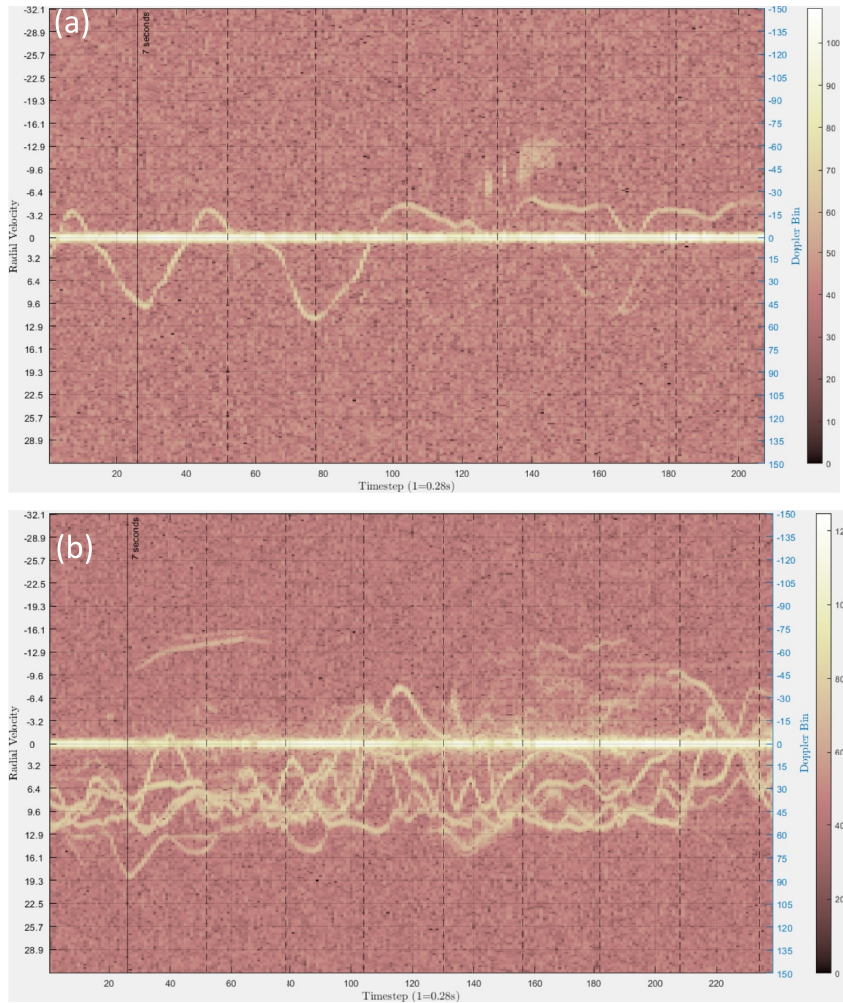


**FIGURE 14** Example spectrograms of a (a) single bird, and (b) flock of birds. The vertical axis is radial velocity in m/s and the colour scale is signal power in dB.

## 6 | RADAR PERFORMANCE BENCHMARKING

### 6.1 | Radar set-up

Currently, each radar operates using its own local conventional reference Oven Controlled Crystal (OCXO) oscillator that is free running with no direct synchronisation between the two radar nodes. The radar can be operated individually as a monostatic system or in a bistatic configuration where one of the radars is transmitting and the other radar is set to receive-only mode by setting its transmit power to zero. The receive-only radar will provide bistatic data using the other radar as its illuminator of opportunity. In this case, the primary radar is operating as a standard monostatic system that both transmits and receives.

The objective is to obtain benchmark performance results from the urban environment with both monostatic and bistatic radar configurations using their conventional oscillators. This provides the basis to repeat measurements with the radar operating with external reference oscillators. The measurements from the radar trials will enable comparative analysis and understanding of the impact of (a) oscillator short-term phase

noise on detection sensitivity in high clutter and (b) oscillator longer-term stability on network synchronisation.

An initial measurement campaign was conducted in July 2022 which is used to generate clutter maps to assess relative performance between the two radars. A second campaign was carried out in September 2022 and data from this trial are used to evaluate the signal power of the I3-D drone from control flights that operated using the process outlined in Section 4.1. First, the benchmark results are reported from the monostatic measurements followed by those with the bistatic data.

### 6.2 | Monostatic radar results

Figure 16 shows a clutter map generated by plotting the zero-Doppler signal as a function of range and azimuth at a fixed altitude. The data are scaled for range and the maps are generated using monostatic range-Doppler data from the elevation beams corresponding to the radar height for each of the two radars. The clutter maps are generated by averaging over 512 frames which roughly equates to approximately 3 min of data. There is a significant overlap between the coverage of

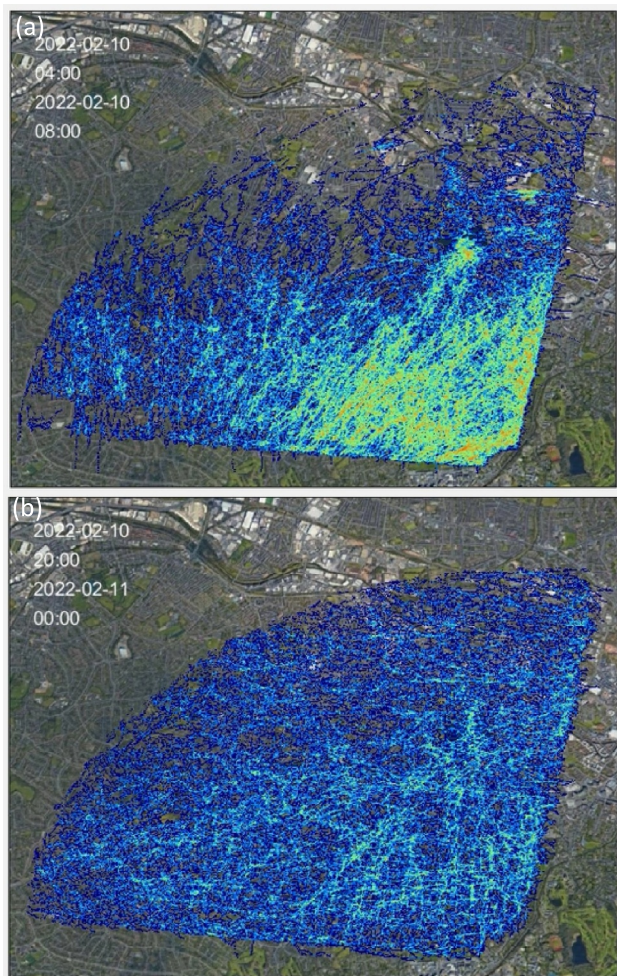


**FIGURE 15** Heatmaps showing bird occupancy over a 4-h period from (a) 04.00 h (GMT) and (b) 20.00 h (GMT). Heatmap data are overlaid onto a map of the area with the colour bar going from blue to yellow to red to show increasing track count.

the two radars (Figure 5(a)) and strong clutter regions visible in both radars are selected for further comparison.

These plots show that there is a much higher level of clutter on the right-hand edges for Radar #1 which corresponds to high-rise city buildings. There are several other regions of strong clutter that correspond to the locations of high-rise buildings. There is one region of strong clutter on the far left that is visible in both plots. This is a multi-storey office block that is in the line-of-site of both radars and provides a good location for comparative measurements of clutter strengths. The building is photographed in Figure 17(a). The Doppler return from this strong stationary clutter is moderately stable over time and is able to provide an estimate of the radar phase noise. Phase noise is defined as the power spectral density measured relative to the carrier in a 1-Hz bandwidth, and is measured in dBc/Hz [14]. For the received data that are at baseband, this is the ratio with respect to the power at zero-Doppler. Thus, in order to compute the phase noise first the mean background power at the specified location is estimated for a range of Doppler frequencies using the same temporal

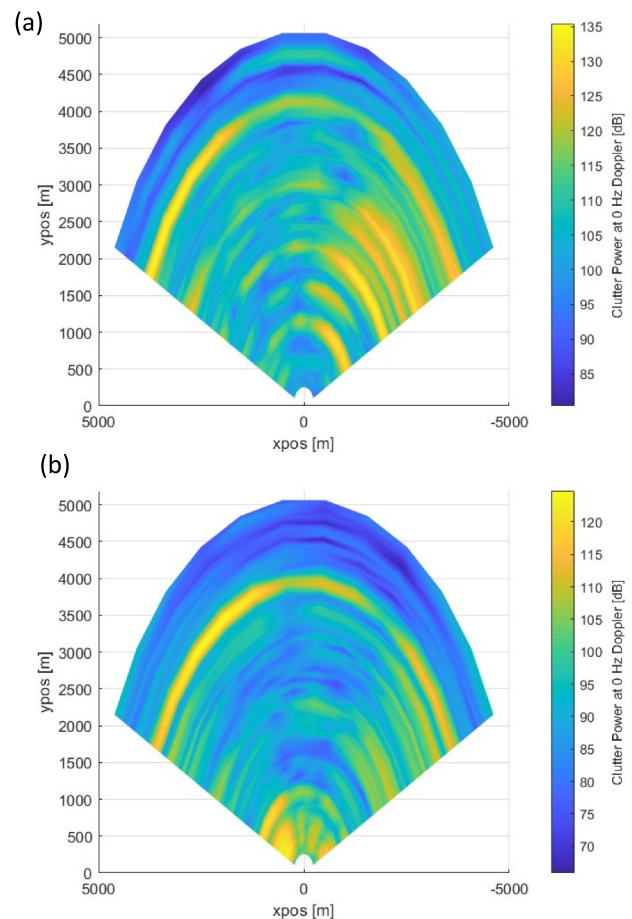


**FIGURE 16** Comparison between the monostatic clutter plots at 0 Hz Doppler for (a) Radar #1 and (b) Radar #2.

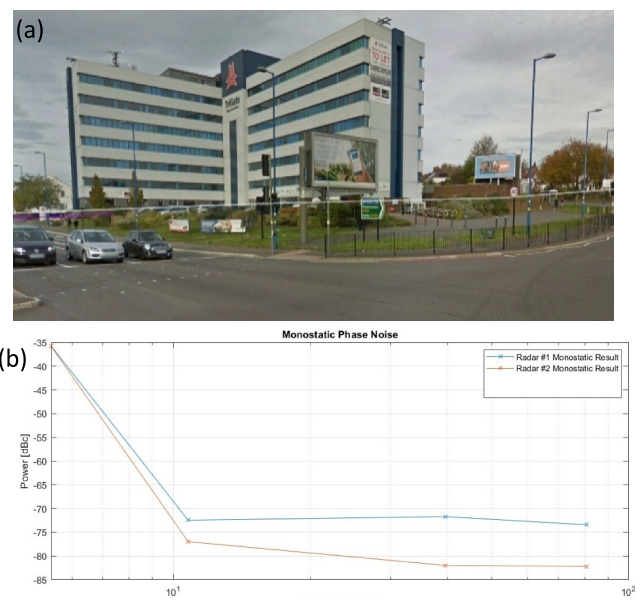


**FIGURE 17** (a) The multi-storey block that yields (b) monostatic phase noise measured with each radar.



averaging process used to obtain the clutter map. Dividing the measured mean power by the zero-Doppler power then gives the phase noise plot as reported in Figure 17b. This result that compares the two monostatic radars shows that Radar #1 has a higher phase noise which implies that the target SNR for this radar is more likely to be clutter-limited.

The impact of the radar's phase noise on target signature quality is further examined by comparing the spectrogram obtained with each radar for the I3-D drone that flew the same pattern clockwise at a constant height of 100 m above ground (Figure 18). Note that both the drone body's echo and the micro-Doppler returns from the drone's rotor blades are more visible in Radar #2. This is in part due to Radar #2 having a higher transmit power. However, what is also noticeable is that in the data from Radar #1 between timeframe 300–500, the background level is raised which is suppressing the target echoes. This is the result of the contribution of phase noise in the presence of high clutter. This is consistent with the result reported in Figure 17b which recorded Radar #1 to have a higher phase noise.

This impact of higher clutter on the noise background is further evident in the corresponding plot comparing the clutter, target and mean noise power that are derived from the

target spectrogram data. From the results plotted in Figure 19, it is evident that the noise floor in Radar #1 is raised for timeframes that report a higher clutter power. This is where the phase noise of the radar is causing the background to become clutter-limited. In comparison, the noise level of Radar #2 is lower and remains so irrespective of the clutter power, implying that the background is at thermal noise power which is consistent with the system having a lower phase noise. Incidentally, Figure 19 is also showing a higher target power for Radar #2 which is consistent with the system operating at a higher transmit power.

### 6.3 | Bistatic radar results

The processing steps for generating the clutter map and target spectrogram from the bistatic measurements are identical to those used with the data except for one crucial difference. Due to the lack of synchronisation in the non-coherent network, the bistatic data must be corrected for Doppler offset due to clock drift and range misalignment as a result of timing offset in the pulse trigger. A software-based method was implemented that uses the direct signal to estimate both of these offsets and

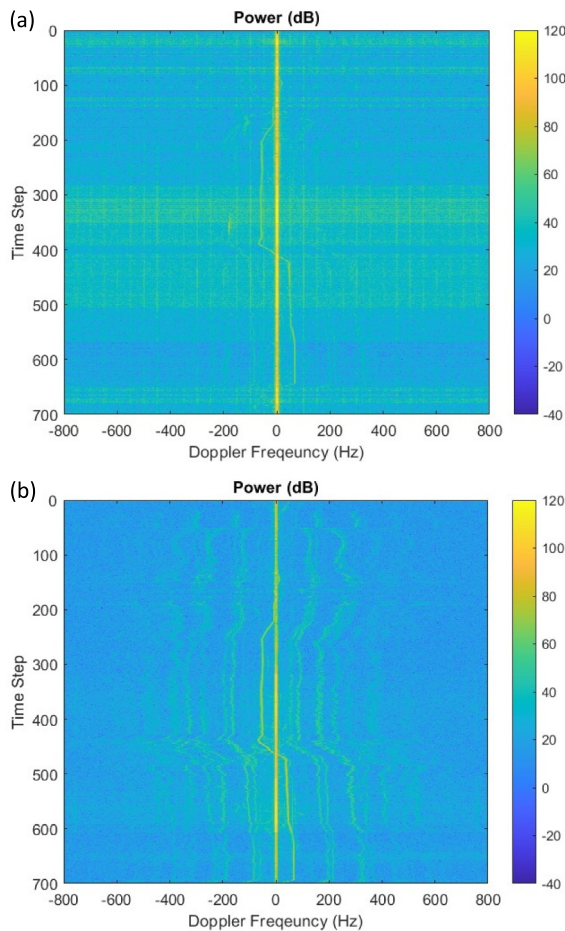


**FIGURE 18** Monostatic spectrograms of the I3-D drone from clockwise flight at 100 m height from (a) Radar #1 and (b) Radar #2.

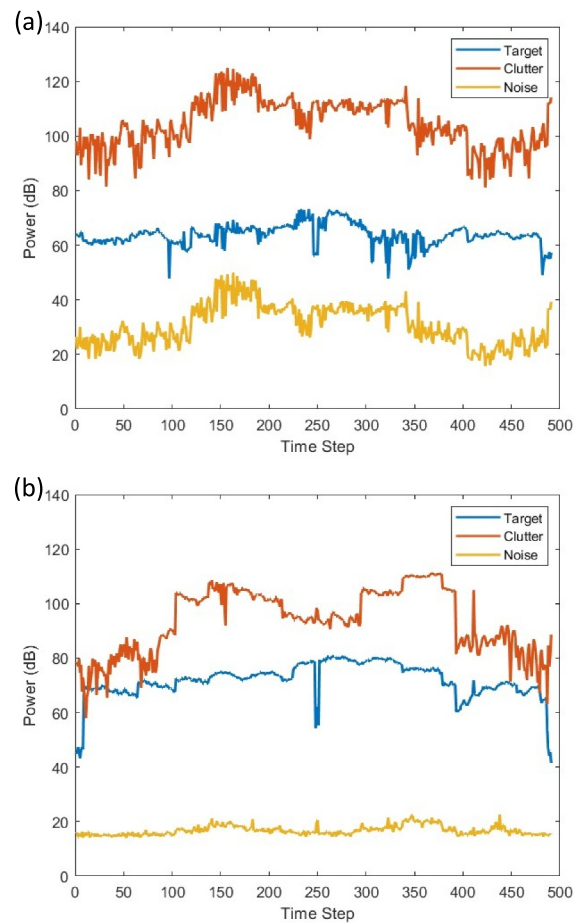


**FIGURE 19** Monostatic result for the I3-D drone target power, clutter power and mean noise power from (a) Radar #1 and (b) Radar #2.



correct the raw data. Griffiths et al. [15] provide full details of the software-based method for correcting the non-coherent data and this was applied to the radar data prior to generating the bistatic clutter maps and target spectrogram data.

Figure 20 compares the bistatic clutter maps between the two radars and these are more similar compared to the equivalent monostatic clutter maps (see Figure 16). This is because the combined bistatic coverage map is very similar and therefore the corresponding clutter maps are more alike. Figure 21 is the corresponding bistatic phase noise measured

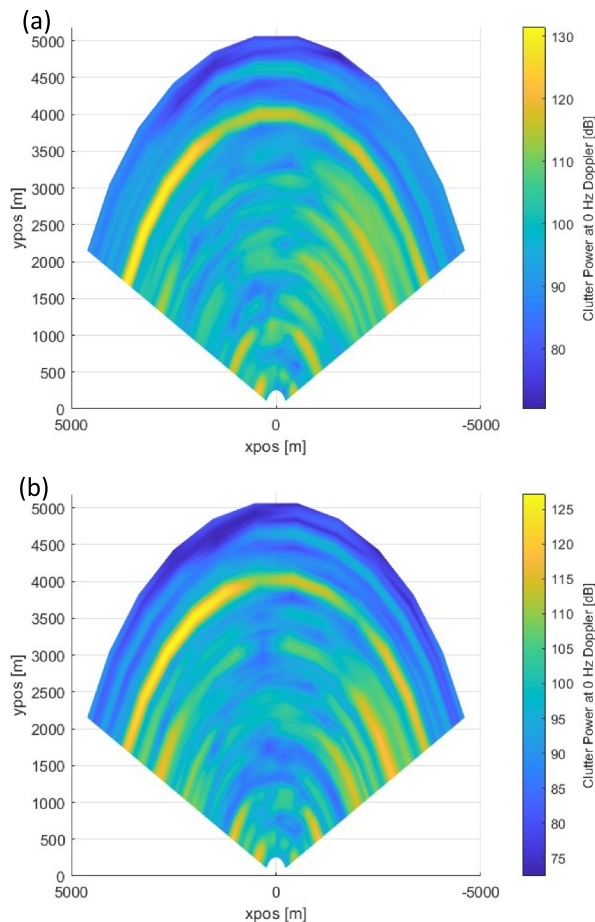


**FIGURE 20** Comparison between the bistatic clutter plots at 0 Hz Doppler from (a) Radar #1 and (b) Radar #2.

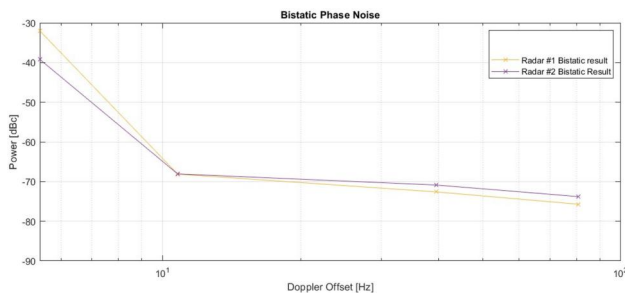


**FIGURE 21** Bistatic phase noise measured with each radar for the location of the multistorey block.

for the multistorey office block. Again, this reflects a combination of the phase noise between the transmit and receive system and the values being closer between the two radars and overall, the phase noise is higher than the monostatic radar. This is again expected as there is no self-cancellation of phase noise in the bistatic configuration which leads to a higher overall phase noise.

This higher phase noise is also evident in the target spectrogram of the bistatic data (Figure 22) from the same flight for which monostatic plots were shown earlier. Note, for example, for Radar #2 for timeframes 300–350 in Figure 22b the background level is raised whereas previously Radar #2 data were on the whole noise-limited for this flight. The same trends can be observed in the plot shown in Figure 23 where the overall noise floor level is higher even though the bistatic clutter power is lower compared to the equivalent monostatic values. This confirms that the phase noise in the bistatic measurements is higher compared to the monostatic values and is in line with that reported in Figure 21 which was estimated using the strong clutter reference point.

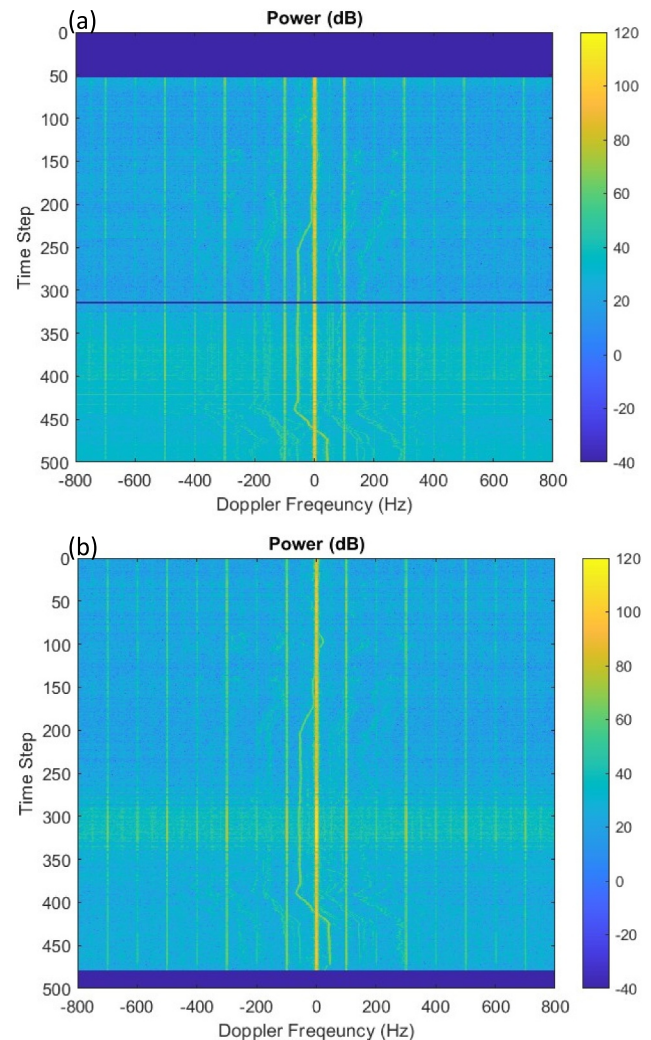


**FIGURE 22** Bistatic spectrograms of the I3-D drone from clockwise flight at 100 m height from (a) Radar #1 and (b) Radar #2.

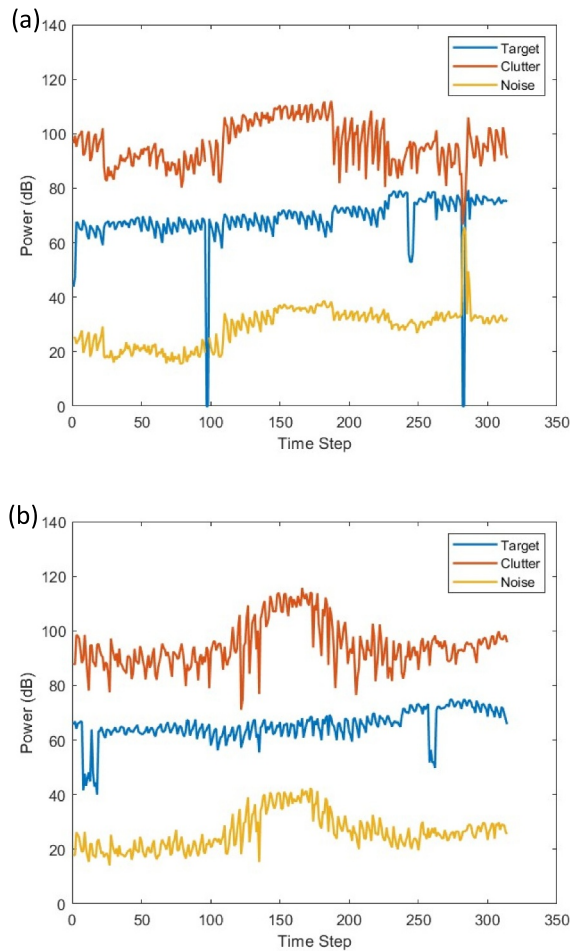


**FIGURE 23** Bistatic results for the I3-D drone target power, clutter power and mean noise power from (a) Radar #1 and (b) Radar #2.

The monostatic and bistatic measurements together provide the necessary benchmark against which the radar performance can be evaluated once changes are made to the radar front end. In the main, these will focus on selecting alternative oscillator sources to operate the radar and the next section describes in further detail the approach being developed at the UoB.

## 7 | EXTERNAL REFERENCE SOURCE HIGH FIDELITY OSCILLATOR

The performance of any clock or frequency standard can be quantified by its instability (i.e. statistical fluctuations of the output frequency) and the uncertainty (i.e. how well the system realises the desired frequency), which are analogous to the typical examples of precision and accuracy, respectively. These Figures of Merit (FoM) are measured in fractional frequency units (i.e. normalised by the output frequency). Allan Deviation is a key FoM used for the measurement of the stability of oscillators and is the deviation of the fractional frequency difference over a specified averaging time. Optical clocks are able to achieve higher performance than microwave clocks, in

both FoM, due to the  $10^5$  factor increase in output frequency, as many of the perturbations and systematic effects are of similar size. For further explanation of Allan Deviation-based FoM, readers are referred to [16].

Typically, the radar will require its oscillator reference source to be operating at microwave frequencies. In the current study, the task of synthesising microwaves from the optical signal is accomplished by a Menlo Microwave generator unit PWMG-1500 (*Menlo-MGU*) ([17, 18]). This system consists of an optical Frequency Comb (*F-Comb*) and an Optical Reference Source (*ORS*) which is an ultra-stable laser operating at 1542 nm. The *F-Comb* is a pulsed laser that is tightly locked to the *ORS* and down-converts the optical frequency to microwave frequency in a phase coherent manner, resulting in little degradation of the phase noise. Microwaves synthesised from a high-quality optical reference enable not only the unrivalled accuracy of optical clocks, but also lower phase noise than traditional microwave sources [19].

A further technological advancement is to operate the optical clock through locking the optical reference frequencies to a well-defined transition between two energy levels within a chosen atom. The UoB is developing a cold-atom based strontium optical lattice clock operating on the 698 nm inter-combination line  $1S_0 \rightarrow 3P_0$  [5]. An ultra-stable laser at this wavelength (Clock Laser) can then be locked to the atomic transition via periodic Rabi spectroscopy [20]. The cold-atom based technique provides a frequency lock relatively slowly, with a linewidth  $< 1$  Hz. Thus, the short-term performance of the system is dominated by the Clock Laser and its longer-term frequency stability is set by the strontium clock. Using telecommunication fibres to transfer the laser signal over a distance requires referencing the Clock Laser to a 1397 nm ultra-stable laser (Transfer Laser), suitable for transmission over the fibre network. The locking operation is performed via second harmonic generation and electronic feedback from the atom lock. However, the transmission of the laser over a fibre link can cause phase noise degradation due to diurnal temperature effects and acoustic noise. These can be minimised by actively stabilising the optical path length of the fibre. An interface node at the Menlo-MGU side will be designed to perform the fibre path length stabilisation and lock the *F-Comb* to the Transfer Laser signal that will replace its internal ORS.

This set-up will then result in a Quantum-enabled radar whereby the radar will operate via a Quantum oscillator. This will replace the radar's conventional internal oscillator with an ultra-low phase noise external reference oscillator. Phase noise results in strong clutter elevating the background level against which moving targets have to be detected. The Quantum oscillator, with its lower close to carrier phase noise, provides the potential to enhance detection of slow-moving weak targets in the presence of strong stationary clutter. For a network set-up a Menlo-MGU unit will be required at each radar node and linked up to the central strontium clock via the phase noise-stabilised fibre network. Whilst the full architecture for the Quantum-enabled radar is depicted in Figure 24, initial development has addressed understanding the oscillator characteristics of the Menlo-MGU and devising the clock transfer

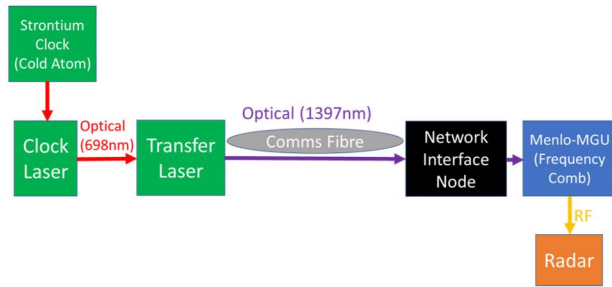


**FIGURE 24** A block diagram illustrating the interface between the Quantum photonics oscillator and the microwave reference source input to the radar.

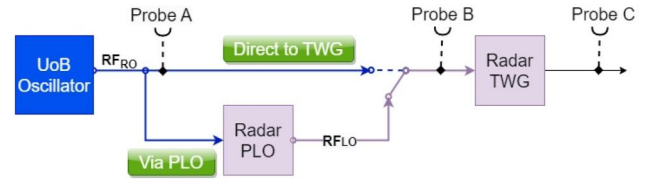
options to establish an interface between the external reference oscillators and the radar.

In terms of the clock transfer option, reference is made to Figure 25 which is a schematic of the front end of the radar. The radar has a Timing and Waveform Generation (TWG) board that controls all of the internal clock timing and generates the carrier frequency signal  $RF_C$ . The TWG takes in a reference local oscillator signal  $RF_{LO}$  which operates at 10s of MHz frequency which is upconverted by the TWG to the L-band  $RF_C$  signal. The TWG board generates a Continuous Wave (CW) output which can be used for monitoring and also a pulse output that is forwarded to a Power Amplifier before it is transmitted through the transmit antenna. The radar provides the  $RF_{LO}$  using a phase Locked Oscillator (PLO) that has a conventional OCXO. The external oscillator is used to provide the external Reference Oscillator ( $RF_{RO}$ ) that can either lock the PLO or input directly to the TWG.

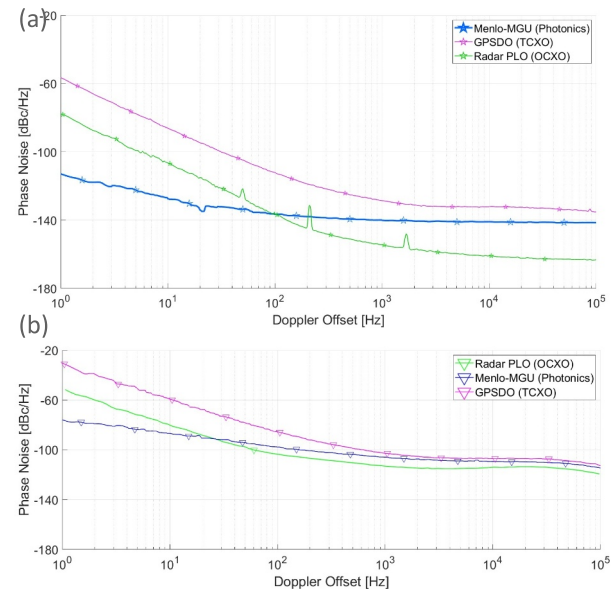
In Figure 25, the markers *Probe B* and *Probe C* are monitoring positions where the RF signal can be measured and assessed for phase noise and related FoM. Using via the *PLO* clock transfer option means that whilst the timing stability is then determined by the external source, the phase noise is still determined by the PLO OCXO. For oscillators that have a smaller phase noise to the radar OCXO, the preferred option is to connect the external oscillator directly to the TWG. Using a stand-alone TWG, the Menlo-MGU and the radar PLO along with one other oscillator were connected to the TWG in turn and the Probe B and Probe C phase noise results reported for comparison. The third oscillator in this instance is a low cost GPS Disciplined oscillator (GPSDO) that has a Temperature Compensated Crystal Oscillator (TCXO). The TCXO on the whole has a higher phase noise compared to the OCXO.

Figure 26 plots the phase noise as a function of Doppler frequency offset from the carrier frequency and is indicative of the residue power at non-zero-Doppler due to static clutter. Both close to carrier and far-out phase noise can impact the detection of weak signals in the presence of strong static clutter.

The phase noise comparisons show that the GPSDO phase noise is higher which is as expected. The Menlo-MGU on the other hand has a lower phase noise at lower offset frequencies although the far-out phase noise is still shown to be lower with the OCXO. Note that the output from the TWG



**FIGURE 25** Schematic of the radar front end illustrating options for interfacing with the external oscillator.



**FIGURE 26** Phase noise bench test measurements for Menlo-MGU, GPSDO and Radar PLO for (a) Probe B at  $RF_{LO}$  and (b) Probe C at  $RF_C$ .

is showing a higher phase noise for all oscillators alike although the far-out phase noise is now much closer suggesting that the TWG white noise is becoming a limiting factor for the upconverted frequencies.

Menlo-MGU, however, provides a number of RF frequencies output and there is an alternative output at 1250 MHz that has a lower phase noise. Hence, another option would be to use this higher frequency and divide it down which can then be used as an alternative signal to input to the TWG. There were a couple of other considerations to take into account regarding configuring the clock transfer option that will have a bearing on the phase noise. First, the ideal input to the TWG is a square wave as it provides sharp zero crossing which reduces the clock jitter on the timing signal that TWG produces from the input reference oscillator signal. Secondly, the radar radome does not have space to accommodate the external oscillators so the RF signal has to be sent via a 10–15 m cable to the TWG in the radar radome. So, the final clock transfer options are as shown in Figure 27 which has two cases:

- (i) the Oscillator Under Test (OUT) being connected via a long cable and passing through a *Squarer* before connecting to the TWG; and



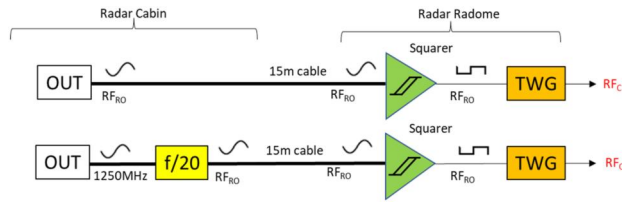


**FIGURE 27** Schematic diagram of the clock transfer option for connecting the external reference OUT with the radar TWG. Top section shows the OUT  $RF_{RO}$  connected via a 15 m cable and a Squarer. The bottom section has an additional Divider which is required when using a higher frequency signal from the OUT.

- (ii) an OUT (in this case the Menlo-MGU) with a 1250 MHz output then passing through a *Divider* to obtain the correct frequency that is then transferred in the same way as (i) to the TWG.

The Divider and the Squarer have been specially designed and built for the radar testbed that minimises the additive phase noise to the OUT. Initial bench tests of the clock transfer configuration have been performed, and the results for the Menlo-MGU are very encouraging (Figure 28). The solid blue curve is the original phase noise measured using the Menlo-MGU  $RF_{RO}$  output and is the same in Figure 26a. The solid red curve is the result obtained taking the 1.25 GHz output after it has been divided down and converted into a square wave. The dashed red line is the phase noise measured directly with the 1250 MHz output signal and scaled to compare all results at the same frequency. The plot shows that the actual achieved phase noise after the Divider and Squarer are slightly higher but it is still showing significant phase noise improvement than the original  $RF_{RO}$  output of the Menlo-MGU. For example, there is 10 dB improvement in phase noise at offset frequencies of 100 Hz which increases to >20 dB of improvement for offset frequencies of 1 kHz and higher. These results show that the Menlo-MGU is providing a lower phase noise compared to OCXO for all except the very far out offset frequencies.

These bench tests have confirmed the ultra-low phase noise properties of the photonics oscillator as obtained from the Menlo-MGU and a viable clock transfer has been proposed to operate the radar testbed using the external reference oscillators.

Additional design changes had to take place with the radar to enable connectivity to external oscillators as the original TWG only operated with an internal oscillator. A modified version of the TWG has been installed in both radars that supports this functionality. A Menlo-MGU unit will be installed in each of the radar stations to provide a photonics-based RF reference source. Future plans are to test the radar with the Menlo-MGU unit and a selection of state-of-art conventional oscillators using the clock transfer option as outlined in Figure 27. These oscillators will be controlled via an RF switch and the phase noise measurements will be repeated with each OUT. Raw radar data from monostatic and bistatic operations will be recorded and the performance of the

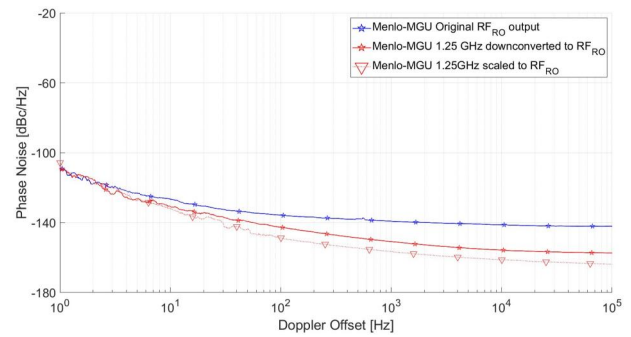


**FIGURE 28** Menlo-MGU phase noise measured at the  $RF_{RO}$  output (solid blue curve), at the output of the 1.25 GHz signal after it has been divided down to  $RF_{RO}$  (solid red curve) and at the 1.25 GHz output which is scaled down numerically (dashed red curve).

networked radar will be compared with the benchmark results reported in Section 6. Once the Quantum oscillator comes on-line, it will be fully integrated into the networked radar. The testbed will provide a unique facility for understanding the impact of ultra-low phase noise highly stable oscillators for the surveillance of low observable targets in demanding realistic urban clutter environments.

## 8 | SUMMARY

This paper describes the radar facility that has been established at the UoB that comprises two L-band staring radars that are installed on the rooftops of two campus buildings. The radars provide overlapping coverage of the city centre of Birmingham and the means of gathering long-term data related to targets in complex realistic clutter. The testbed is operating as a network of two staring radars and example results for detecting drones and birds as targets are reported to illustrate the work from ongoing measurement campaigns and include reference to recent published work based on data from the UoB testbed. Additionally, a full set of benchmark results is provided for monostatic and bistatic urban measurement whilst operating the radar with their existing conventional oscillators that form a basis of performance comparison for future tests involving external oscillators.

Future developments are outlined that will see the integration of a range of state-of-art oscillators leading to the formation of a fully coherent network of two staring radars and bench test performance results are reported for both conventional and photonics oscillators to begin with. With the completion of the network set-up, the radar infrastructure provides an ideal platform for long-term studies of monostatic and multistatic performance in a challenging urban environment. It will contribute to understanding the impact of photonics and Quantum oscillators on radar performance and networking capabilities. The data from this facility will be invaluable in optimising detection, tracking and classification algorithms for a host of applications, including counter-drone defence, monitoring of future air space usage and aeroecology.

## AUTHOR CONTRIBUTION

**Mohammed Jahangir:** Conceptualization; Data curation; Methodology; Validation; Visualization; Writing – original draft. **Darren Griffiths:** Data curation; Software; Validation; Visualization; Writing – review & editing. **Daniel White:** Data curation; Software; Visualization; Writing – review & editing. **Gwynfor Donlan:** Data curation; Writing – review & editing. **Xiaofei Ren:** Data curation; Writing – review & editing. **Jithin Kannanthara:** Data curation; Writing – review & editing. **Yeshpal Singh:** Conceptualization; Funding acquisition; Writing – review & editing. **Joseph P. Wayman:** Data curation; Visualization; Writing – review & editing. **Chris J. Baker:** Funding acquisition; Writing – review & editing. **Jon P. Sadler:** Funding acquisition; Writing – review & editing. **S. James Reynolds:** Funding acquisition; Writing – review & editing. **Michail Antoniou:** Funding acquisition; Methodology; Supervision; Writing – review & editing.

## ACKNOWLEDGEMENTS

The work is funded by the UK National Quantum Technology Hub in Sensing and Timing (EP/T001046/1) and the EPSRC MEFA (EP/T011068/1) projects. The authors are grateful to Thales for helping with installing the radar and their ongoing engagement with the research work supported by the testbed.

## CONFLICT OF INTEREST STATEMENT

All the authors declare no conflict of interest.

## DATA AVAILABILITY STATEMENT

The data that support the findings of this study are available from the corresponding author upon reasonable request.

## ORCID

*Mohammed Jahangir*  <https://orcid.org/0000-0002-5847-380X>

*Darren Griffiths*  <https://orcid.org/0000-0003-3194-439X>

*Jithin Kannanthara*  <https://orcid.org/0000-0002-6156-1181>

## REFERENCES

1. Clemente, C., et al. (eds.): Radar Countermeasures for Unmanned Aerial Vehicles. The IET, Institution of Engineering and Technology (2021)
2. Lee, J., Byun, Y.S.: Analysis of clutter cancellation capability considering radar system phase noise effects. In: IEEE Antennas and Propagation Society International Symposium 1997, vol. 4, pp. 2442–2445 (1997)
3. Oswald, G.A.K.: Holographic surveillance radar, Proc. SPIE 7308. Radar Sensor Technology, 73080D (2009)

4. Jahangir, M.: Target Centric Wide-Area 3-D Surveillance Using a Non-scanning Multibeam Receiver Array, pp. 652–657. IEEE Radar 2015, Arlington (2015)
5. Jahangir, M., et al.: Development of Quantum Enabled Staring Radar with Low Phase Noise. EuRAD 2021, London (2022)
6. Sim, J., et al.: Effective ground-truthing of supervised machine learning for drone classification. In: Intern. Radar Conf. 2019 (2019)
7. Nigam, N., Dutta, T., Gupta, H.: Impact of Noisy Labels in Learning Techniques: A Survey, pp. 403–411 (2020). [https://doi.org/10.1007/978-981-15-0694-9\\_38](https://doi.org/10.1007/978-981-15-0694-9_38)
8. White, D., et al.: Multi-rotor drone micro-Doppler simulation incorporating genuine motor speeds and validation with L-band staring radar. In: IEEE Intern. Radar Conf. 2022. New York (2022)
9. Jahangir, M., et al.: Measurements of Birds and Drones with L-Band Staring Radar. IRS 2021, Berlin (2021)
10. Dale, H., et al.: Convolutional Neural Networks for Drone Model Classification. EuRAD 2021, London (2022)
11. Dale, H., et al.: SNR-dependent drone classification using convolutional neural networks. IET Sonar Radar and Navig 16, 1–12 (2021). <https://doi.org/10.1049/rsn2.12161>
12. Dale, H., et al.: Convolutional neural networks for robust classification of drones. In: IEEE Intern. Radar Conf. (2022)
13. Wayman, J.P., et al.: L-band radar quantifies major disturbance of birds in an urban area. Sci. Rep. 13(1), 12085 (2023). <https://doi.org/10.1038/s41598-023-39223-1>
14. Rubiola, E.: Phase Noise and Frequency Stability in Oscillators, vol. 20010, pp. 2012. Cambridge University Press (2008)
15. Griffiths, D., et al.: Direct Signal Synchronization for Staring Passive Bi-static Radar. IET Radar Conference 2022, Edinburgh (2022)
16. Riley, W., Howe, D.: Handbook of Frequency Stability Analysis. Special Publication (NIST SP), National Institute of Standards and Technology, Gaithersburg (2008). [online]. [https://tsapps.nist.gov/publication/get\\_pdf.cfm?pub\\_id=50505](https://tsapps.nist.gov/publication/get_pdf.cfm?pub_id=50505). Accessed 12 October 2023
17. Menlo Systems GmbH. PMWG 1500 product web page," [Online]. <https://www.menlosystems.com/products/ultrastable-microwaves/pmwg-1500/>. Accessed Mar 2023
18. Bradler, M., et al.: Photonic microwave generator as quantum local oscillator for radars. In: Joint Conf. Europ. Freq. & Time Forum and IEEE Intern. Freq. Control Symposium 2022, 24–28 (2017)
19. Xie, X., et al.: Photonic microwave signals with zeptosecond-level absolute timing noise. Nat. Photonics 11(1), 44–47 (2017). <https://doi.org/10.1038/nphoton.2016.215>
20. Knight, P., Milonni, P.W.: The Rabi frequency in optical spectra. Phys. Rep. 66(2), 21–107 (1980). [https://doi.org/10.1016/0370-1573\(80\)90119-2](https://doi.org/10.1016/0370-1573(80)90119-2)

**How to cite this article:** Jahangir, M., et al.: Development of a networked photonic-enabled staring radar testbed for urban surveillance. IET Radar Sonar Navig. 1–15 (2023). <https://doi.org/10.1049/rsn2.12524>